

Physical properties of new delafossite triangular-lattice compounds TlErSe_2 and TlTmSe_2

Bastian Rubrecht,¹ Ellen Häußler,² Mirtha Pillaca,² Pritam Bhattacharyya,³ Liviu Hozoi,³ Artem Nosenko,^{1,4} Dmitri V. Efremov,¹ Bernd Büchner,^{1,5} Anja U.B. Wolter,¹ and Thomas Doert²

¹*Institute for Solid State Research, Leibniz IFW Dresden, Helmholtzstraße 20, 01069 Dresden, Germany*

²*Faculty of Chemistry and Food Chemistry, Technische Universität Dresden, 01062 Dresden, Germany*

³*Institute for Theoretical Solid State Physics, Leibniz IFW Dresden, Helmholtzstraße 20, 01069 Dresden, Germany*

⁴*Kyiv Academic University, 03142 Akademika Vernads'koho Blvd., 36, Kyiv, Ukraine*

⁵*Institute of Solid State and Material Physics and Würzburg-Dresden Cluster of Excellence ct.qmat, Technische Universität Dresden, 01062 Dresden, Germany*

(Dated: December 15, 2025)

Delafossite compounds containing rare-earth ions have been proven to be an ideal platform to investigate frustrated magnetic ground states. Here, we discuss two triangular-lattice antiferromagnets, TlErSe_2 and TlTmSe_2 , as potential candidates for hosting exotic quantum states. Powder X-ray diffraction data analysis of the black-color polycrystalline TlRESe_2 (RE : Er and Tm) samples confirms the phase purity. Both materials crystallize in the trigonal $\alpha\text{-NaFeO}_2$ structure ($R\bar{3}m$) with lattice parameters $a = 4.1070(4)$ Å and $c = 23.1472(1)$ Å for the erbium compound and $a = 4.0916(1)$ Å and $c = 23.1483(2)$ Å for the thulium compound. Magnetic susceptibility measurements show an effective moment of $\mu_{\text{eff}} = 9.6(2) \mu_B/\text{f.u.}$ ($7.5(1) \mu_B/\text{f.u.}$) for TlErSe_2 (TlTmSe_2) for temperatures above 200 K. While ^3He specific-heat measurements reveal long-range magnetic order below $T_N = 0.42$ K for TlErSe_2 , no sign of long-range magnetic order was observed for TlTmSe_2 . Based on our results, we map out the T-H phase diagram for polycrystalline TlErSe_2 and discuss the striking difference in the magnetic behavior of TlTmSe_2 based on our ab initio quantum chemical calculations.

I. INTRODUCTION

Frustration lies at the heart of a variety of exotic magnetic ground states and responses in solid state magnetism. It can be of pure geometric nature as for the Heisenberg antiferromagnetic triangular lattice or can arise from competing anisotropic interactions as in Kitaev's honeycomb model. In some systems it may actually imply both geometric frustration and peculiar anisotropic couplings, e. g., on triangular lattices of edge-sharing MX_6 octahedra, where M stands for a d - or f -electron ion and X for chalcogen or halide species. Illustrative examples of such edge-sharing networks of MX_6 octahedra are triangular Kitaev-Heisenberg like CoI_2 [1], NaRuO_2 [2], and CsCeSe_2 [3] or Ising antiferromagnets with 'intrinsic' transverse fields like TmMgGaO_4 [4–7] and KTmSe_2 [8]. The former provide the playground for studying quantum spin liquid (QSL) physics [2], the latter are of interest in relation to Berezinskii-Kosterlitz-Thouless (BKT) phases [9, 10].

Rare-earth delafossites with the chemical formula AMX_2 emerge in this context as a versatile material platform that allows to investigate both QSL and BKT states. Though the role of Kitaev exchange is not yet fully clarified in some cases, potential QSL ground states were pointed out in both $\text{Yb}^{3+} 4f^{13}$ [11–21] and $\text{Ce}^{3+} 4f^1$ [22] delafossites while the structurally related $\text{AMX}_2 4f^{12}$ compounds represent promising potential BKT systems, since ambiguities arising from Mg-Ga intermixing and associated disorder as encountered in the TmMgGaO_4 material [4–7] are circumvented in the delafossite architecture.

Here we report the synthesis and investigation of both odd- and even-electron new compounds in the $4f^n$ delafossite series, displaying the same ligand and A-site matrix — TlErSe_2 and TlTmSe_2 . The former features $\tilde{S}=1/2$ magnetic moments related to a Kramers-doublet ground state at each $4f^{11}$ site and is found to order antiferromagnetically below 420 mK. No sharp phase transition is observed in the latter material; its low-energy multiplet structure, characterized by two nearly degenerate singlet states at each $4f^{12}$ center, is discussed in relation to the transverse field Ising model [6, 7, 10]. Our results add new reference points within the landscape of late rare-earth triangular-lattice magnetic systems. Studies on A=Tl delafossites, in particular, are scarce, likely due to the toxicity of thallium — besides early works focusing on structural aspects or which were limited to temperature $T \geq 4.2$ K [23–25], only the magnetism of the $4f^{13}$ Kramers-ion systems TlYbS_2 [26] and TlYbSe_2 [21] has been addressed so far. Our work provides valuable insights into this particular direction.

II. EXPERIMENTAL AND COMPUTATIONAL METHODS

Synthesis. Due to the air and moisture sensitivity of the starting materials and products, all the experimental work was carried out in an Ar-filled glove box with O_2 and H_2O levels below 0.1 ppm. Polycrystalline TlErSe_2 and TlTmSe_2 samples were synthesized in two steps via the solid state method by using high purity elements of Tl (Alfa Aesar, 99.9%), Erbium (Mateck, 99.5 %), Thulium

(Mateck, 99.99 %), and Se (Chempur, 99.999%, reduced in H_2 stream at 400 °C) as raw materials.

Firstly, the Tl_2Se precursor was synthesized from a stoichiometric mixture 2:1 of Tl and Se in an evacuated ($\sim 10^{-3}$ mbar) sealed quartz ampule. The ampule was placed in a muffle furnace (Nabertherm), heated up to 500 °C with a ramp of 100 K/h, kept at this temperature for 24 h, and finally cooled down to room temperature within 5 hours.

In the second step, polycrystalline $TlErSe_2$ and $TlTmSe_2$ were synthesized out of a stoichiometric mixture of Tl_2Se , Se, and Er or Tm, respectively. The three components were weighted in a molar ratio of 1:2:3, mixed in an agate mortar, and placed in a glassy-carbon crucible inside a quartz ampule of 16 mm diameter. The evacuated ampule was heated to 500–540 °C with a heating rate of 100 K/h and dwelled for 24 hours. Afterward, the ampule containing $TlTmSe_2$ was cooled down with 10 K/h, and the ampule containing $TlErSe_2$ was water quenched. Both obtained samples were pulverized for further structural and physical properties characterization.

In addition, a non-magnetic reference material, $TlLuSe_2$, was synthesized in polycrystalline form following a similar procedure.

Powder X-Ray diffraction. The phase purity of the prepared samples was checked by powder X-ray diffraction (PXRD) with an Empyrean diffractometer (PANalytical, $Cu-K\alpha_1$ radiation) equipped with a Ge(111) monochromator. The data were collected in a Bragg-Brentano setup in the 2θ -range of 5 to 90°. For the accurate lattice parameters measurement, the samples were mixed with a small amount of Si powder (NIST SRM 640c, $a = 5.43119(1)\text{\AA}$) as an internal standard. Lattice parameters of the samples were determined by Rietveld refinement using the TOPAS Academic software [27, 28].

Magnetization and heat capacity. Magnetization and specific heat measurements were performed on pressed pellets of the polycrystalline sample. DC magnetometry was performed using a Superconducting QUantum Interference Device (SQUID) magnetometer from Quantum Design (MPMS 3) for fields up to 7 T and a Physical Property Measurement System (PPMS) for magnetic fields up to 14 T, both equipped with a Vibrating Sample Magnetometer (VSM) option.

The specific heat was measured using the relaxation method with a PPMS equipped with a 3He refrigerator option. The background signal of the sample holder was measured separately and then subtracted. The lattice contribution to the specific heat was approximated by the Lindeman-scaled isostructural non-magnetic analogue $TlLuSe_2$.

Band structure DFT computations. First-principles calculations were conducted to investigate the electronic structures of $TlErSe_2$ and $TlTmSe_2$. The *ab initio* simulations were performed using the projector augmented-wave (PAW) method [29], as implemented in the Vi-

enna *Ab initio* Simulation Package (VASP) [30, 31]. An energy cutoff of 700 eV was applied to the plane-wave basis set. The Brillouin zone was sampled using a Γ -centered $28 \times 28 \times 28$ k-point mesh. Spin-orbit coupling (SOC) was included self-consistently in all calculations. The *f*-electrons of Er and Tm were treated as core electrons. For both compounds the trigonal crystal structure (sg 166) together with the experimentally obtained lattice parameters were used. The crystal structure parameters are $a = 4.0916(1)\text{\AA}$ and $c = 23.1483(2)\text{\AA}$ for $TlTmSe_2$ and $a = 4.1070(4)\text{\AA}$ and $c = 23.1472(1)\text{\AA}$ for $TlErSe_2$. All calculations assumed non-magnetic configurations. For post-processing we used the pymatgen python library [32].

Quantum chemical calculations. *ab initio* quantum chemical calculations for the multiplet structures of both compounds, $TlErSe_2$ and $TlTmSe_2$, were carried out using the ORCA [33, 34] and MOLPRO [35] programs, respectively. For this purpose, clusters consisting of one central $ErSe_6/TmSe_6$ octahedron, six adjacent Er/Tm sites, and 12 Tl nearest-neighbor cations were considered. The crystalline environments were modeled as large arrays of point charges which reproduce the crystalline Madelung field within the cluster volume; we employed the EWALD program [36, 37] to generate the point-charge embeddings. The performance of such an embedded-cluster quantum chemical approach for the case of 4*f*-electron compounds is discussed in e. g. [38, 39].

The quantum chemical investigation was initiated as complete active space self-consistent field (CASSCF) computations [40] with active orbital spaces containing the seven 4*f* orbitals of the central Er/Tm ion. Post-CASSCF calculations were performed for the $TlTmSe_2$ system at the level of multireference configuration-interaction (MRCI) with single and double excitations [40, 41] out of the Tm 4*f* and Se 4*p* orbitals of the central $TmSe_6$ octahedron. The spin-orbit (SO) interaction matrix was computed for the lowest 11 spin triplet (out of a total number of 21) and nine spin singlet (out of a total number of 28) $4f^{12}$ states. Other higher-lying triplet and singlet $4f^{12}$ states have relative energies that are respectively larger by ≈ 1 and ≈ 2.4 eV, in the calculation without SOC; excluding those from the SO treatment does not significantly affect the low-energy $4f^{12}$ relativistic spectrum in $TlTmSe_2$, as illustrated at CASSCF level in the Appendix (Tab. V).

With three holes in the 4*f* subshell, MRCI is computationally too expensive for the $TlErSe_2$ compound. Post-CASSCF calculations were therefore performed for $TlErSe_2$ at the level of *N*-electron valence second-order perturbation theory (NEVPT2) [42]. All possible states (35 quartets and 112 doublets) derived from the $4f^{11}$ valence configuration were included in the SO treatment either at CASSCF or NEVPT2 level.

The basis sets used in the computational study are described in the Appendix.

III. RESULTS

The powder X-ray diffraction pattern based Rietveld analysis, shown in Fig. 1, confirms the single-phase formation of the polycrystalline TlErSe_2 and TlTmSe_2 compounds with the rhombohedral $\alpha\text{-NaFeO}_2$ structure and space group $R\bar{3}m$ (No. 166). Tl^{1+} , RE^{3+} , and Se^{2-} atoms occupy the Wyckoff position (and atomic coordinates) $3b$ (0, 0, 0.5), $3a$ (0, 0, 0) and $6c$ (0, 0, z), respectively. Therefore, during the refinement analysis, only the z coordinate of the Se atom was refined. Lattice parameters as well as the reliability factors of both compounds obtained are shown in Table I. They are in good agreement with the values reported by Duczmal *et al.* [25, 43], but quite different from the ones reported by Kabre *et al.* [23]. This difference may be related to the fact that in Ref. [23] the lattice parameters determination was done over 12 diffraction peaks only. The lattice parameters of the isostructural and non-magnetic reference TlLuSe_2 are $a = 4.0656(7)\text{\AA}$, $c = 23.1769(4)\text{\AA}$, and $V = 331.77(1)\text{\AA}^3$. The isotropic thermal displacement parameters B_{eq} were kept fixed at 1.0\AA^2 and the site occupancies were also fixed to 1.0 in the refinements and structural parameters of the Rietveld fits are summarized in Table I. Furthermore, energy dispersive X-ray (EDX) analysis and inductively coupled plasma optical emission spectroscopy (ICP-OES) measurements in the powder sample of TlErSe_2 and TlTmSe_2 confirm the homogeneity and stoichiometric composition of the delafossite compounds.

The refined crystal structures of TlErSe_2 and TlTmSe_2 are shown in Fig. 2, in which the stacked layered ErSe_6 and TmSe_6 octahedra are arranged in an ABC sequence and separated by 7.718\AA and 7.7116\AA , respectively. The bond lengths and angles of the slightly distorted ErSe_6 and TmSe_6 octahedra together with a single layer of Er/Tm atoms ordered in a perfect triangular lattices are also indicated.

Fig. 3 a) shows the magnetization of TlErSe_2 divided by the applied field (M/H) as a function of temperature in an external magnetic field of 1 T. The data was fitted with the Curie-Weiss law, i.e., $M/H(T) = C/(T - \Theta_{CW})$, for temperatures above 200 K. The corresponding fitting yields an effective moment of $\mu_{\text{eff}} = 9.6 \pm 0.2\mu_B/\text{Er}$ and a Curie-Weiss temperature of $\Theta_{CW} = -(7 \pm 1)\text{K}$. The effective moment is in good agreement with the expected value for a trivalent free Er -ion of $\mu_{\text{eff}} = 9.58\mu_B$ [45]. Similar results have been found in other Er -based delafossites such as NaErSe_2 and KErSe_2 , where a $\mu_{\text{eff}} = 9.5\mu_B$ was reported for both compounds [46]. The negative Θ_{CW} indicates sizable antiferromagnetic correlations between the Er^{3+} ions. Down to the lowest measured temperature of 1.8 K no sign of ordering is observed, resulting in a minimal frustration factor $f = |\Theta_{CW}/T_N|$ [47] of ≈ 3.9 . The insert shows M/H as a function of the temperature for applied fields $\geq 2\text{ T}$ and its first derivative. dM/dT reveals a minimum at 3.2 K and 2 T, that shifts towards higher temperatures and broadens with increas-

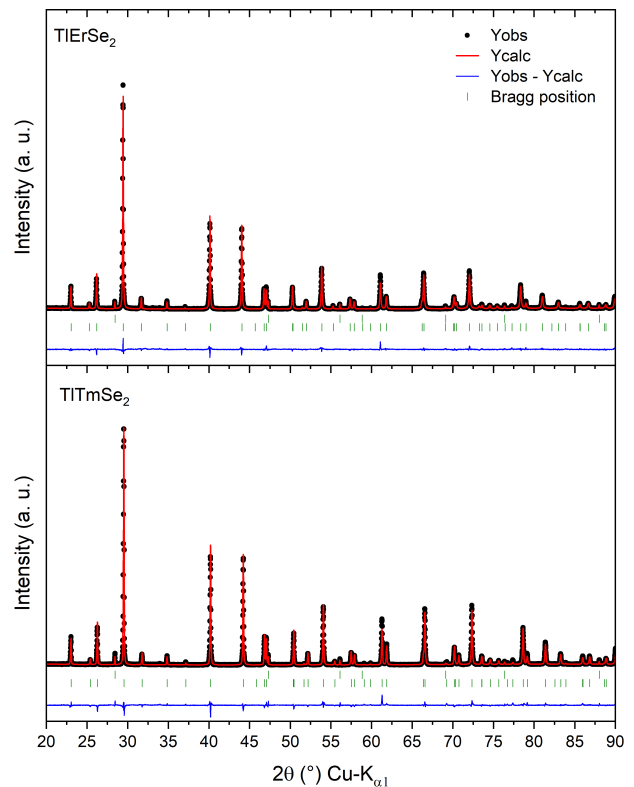


Figure 1. PXRD pattern with Rietveld refinement analysis for TlErSe_2 (top) and TlTmSe_2 (bottom) sample. Solid black circles are observed intensities, red lines are the calculated intensities, and blue lines are the difference between the observed and the calculated intensities. Short vertical lines show the position of Bragg reflections for TlErSe_2 and TlTmSe_2 , respectively as well as for Si (internal standard).

ing applied field. This minimum is taken as an indication of the gradual field polarization (see Fig. 11). This observation agrees well with the field-dependent measurement of the magnetization (Fig. 4 a). At low temperatures, the moment first steeply increases with an increasing field and then slowly tapers off becoming almost linear for applied fields greater than $\sim 10\text{ T}$, finally reaching $\sim 6.5\mu_B/\text{Er}$ at 14 T and 2 K.

Fig. 3 b) shows the temperature dependence of the magnetization divided by the applied magnetic field for TlTmSe_2 . The data show no evidence of a magnetic transition in TlTmSe_2 down to 1.8 K. M/H follows a Curie-Weiss law above 200 K. The fit yields an effective moment of $\mu_{\text{eff}} = (7.5 \pm 0.1)\mu_B/\text{Tm}$ and a Curie-Weiss temperature of $\Theta_{CW} = (-10 \pm 2)\text{K}$. The obtained effective moment is in good agreement with the theoretical moment of free Tm^{3+} ion ($7.57\mu_B$) [45]. Θ_{CW} indicates sizable antiferromagnetic correlations. The resulting frustration factor is at least $f \geq 5$. At around $\sim 100\text{ K}$ the magnetic behavior starts to deviate from the Curie-Weiss law with the observed magnetization being smaller than the free ion value, indicating a reduction of the Curie constant C

Table I. Rietveld results of structural parameters, atomic coordinates (x, y, z), and equivalent isotropic displacement parameters (B_{eq}). Residual factors are $R_p(\%) = 7.31$, $R_{wp}(\%) = 9.71$, $R_{exp}(\%) = 4.82$, and the goodness-of-fit is $GoF = 2.02$ for $TiTiSe_2$ and $R_p(\%) = 5.40$, $R_{wp}(\%) = 7.10$, $R_{exp}(\%) = 4.89$, and $GoF = 1.45$ for $TiErSe_2$.

Lattice parameters	Atom	Wyckoff position	x	y	z	Occupancy	$B_{eq}(\text{\AA}^2)$
$a = 4.1070(4) \text{ \AA}$	Er	$3a$	0	0	0	1.0	1.0
$c = 23.147(1) \text{ \AA}$	Ti	$3b$	0	0	1/2	1.0	1.0
$V = 338.13(7) \text{ \AA}^3$	Se	$6c$	0	0	0.267(1)	1.0	1.0
$a = 4.0916(1) \text{ \AA}$	Tm	$3a$	0	0	0	1.0	1.0
$c = 23.1483(2) \text{ \AA}$	Ti	$3b$	0	0	1/2	1.0	1.0
$V = 335.602(6) \text{ \AA}^3$	Se	$6c$	0	0	0.2657(5)	1.0	1.0

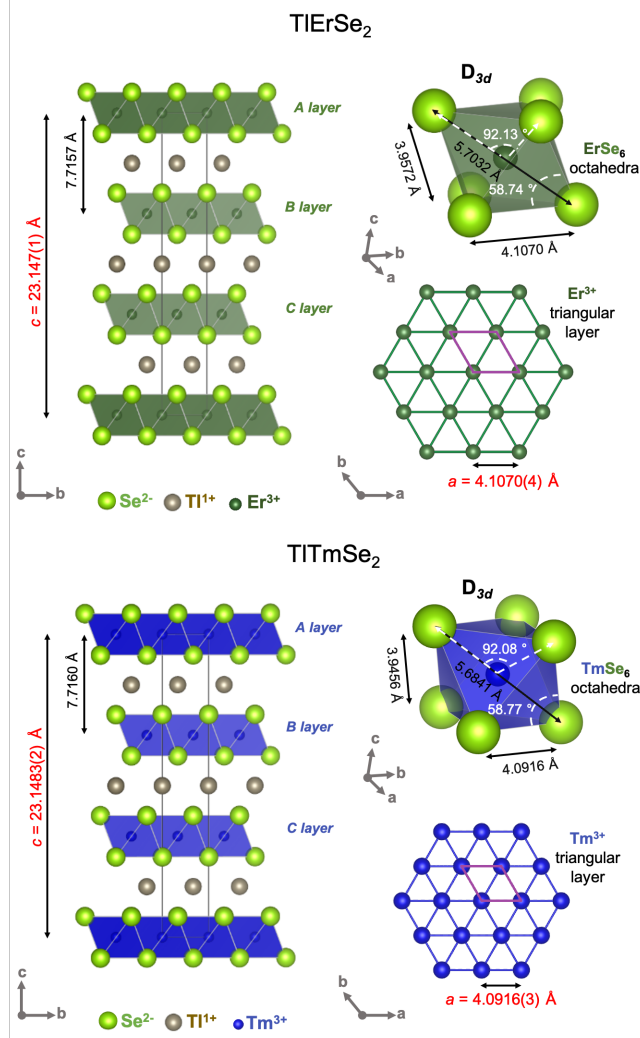


Figure 2. Refined crystal structures of $TiErSe_2$ and $TiTmSe_2$ with space group $R\bar{3}m$. The $ErSe_6$ and $TmSe_6$ distorted-octahedra with D_{3d} structure and the diagram of a single perfect triangular layer of Er^{3+} and Tm^{3+} ions (viewed along the c -axis) are also shown. The unit cells are indicated with solid purple lines. Ti^{1+} , Er^{3+}/Tm^{3+} , and Se^{2-} atoms are shown in brown, green/blue, and light green, respectively. Illustrations were generated in VESTA [44].

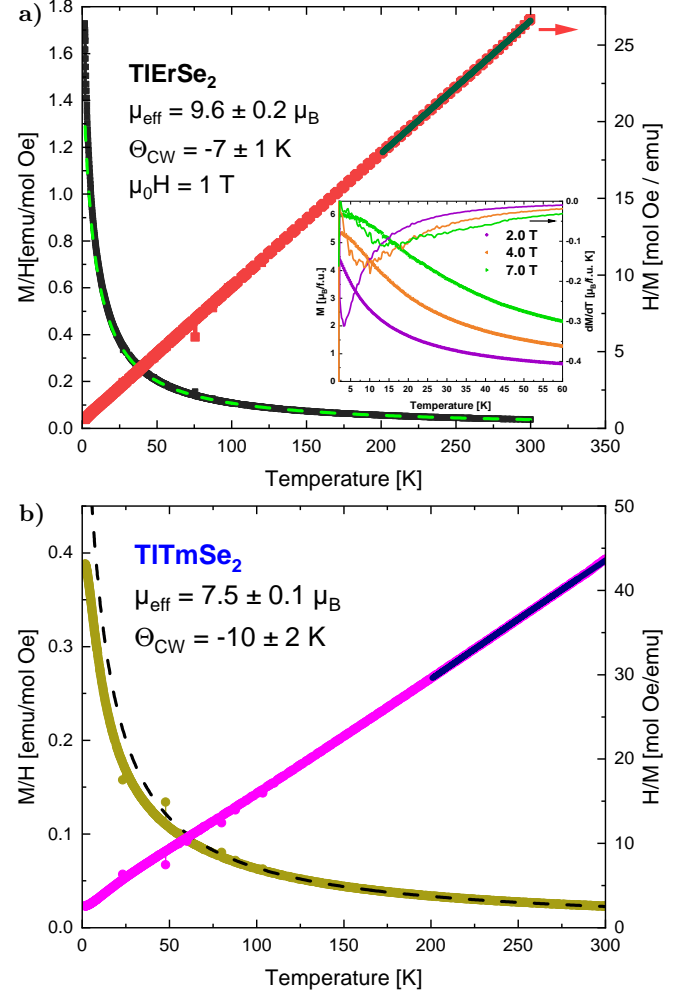


Figure 3. a) Temperature dependence of the magnetization of $TiErSe_2$ divided by the applied field (M/H) and its inverse. The insert shows the temperature dependence of the magnetization and its first derivative of $TiErSe_2$ for applied fields of 2, 4, and 7 T. b) M/H and its inverse of $TiTmSe_2$ as a function of temperature measured at 1 T. The solid lines correspond to a Curie-Weiss fit for temperatures above 200 K.

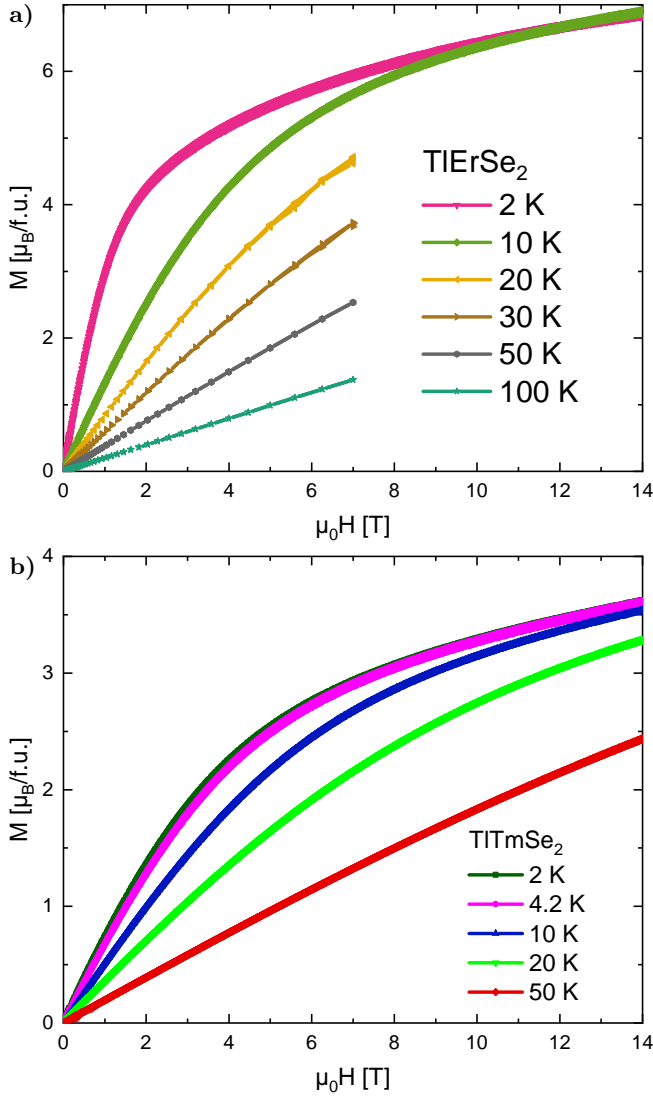


Figure 4. a) Field dependence of the magnetic moment per formula unit of TlErSe_2 a) and TlTmSe_2 b) for various temperatures.

as a function of temperature.

Isothermal magnetization data of TlTmSe_2 collected at various temperatures are plotted in Fig. 4 b). The low-temperature data shows a steep increase of the magnetic moment over the first three Teslas up to $\sim 2 \mu_B/\text{f.u.}$, which then slowly transitions into a linear behavior for fields greater than ~ 12 T. The linear behavior above ~ 12 T may at least partly be attributed to a temperature-independent van-Vleck contribution stemming from excitations to higher CEF level.

It should be noted, however, that the measured samples are polycrystalline and thus the observed finite linear slope at high field may originate not purely from a van-Vleck contribution but from the polycrystalline average. Rare-earth magnets in general, but also more specifically rare-earth-based delafossites commonly display a large g -factor anisotropy [46, 48–50]. The presented data is a

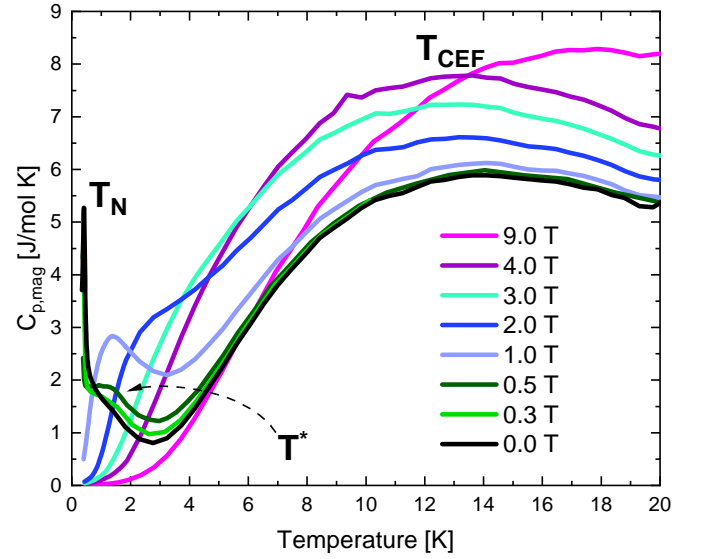


Figure 5. Magnetic contribution of the specific heat $C_{p,\text{mag}}$ as a function of temperature for various magnetic fields. T_N marks the transition temperature and T^* corresponds to the shoulder-like feature in addition to the broad maximum T_{CEF} from populated higher CEF level.

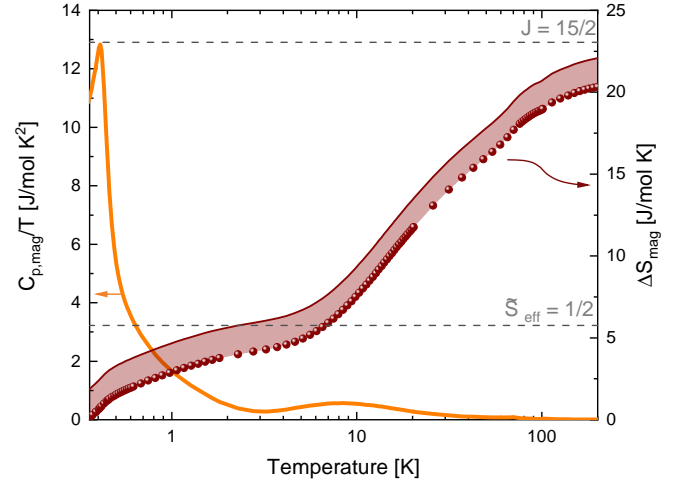


Figure 6. Magnetic contribution of the specific heat divided by temperature $C_{p,\text{mag}}/T$ of the zero field measurement (orange solid line, left y -axis) and the corresponding integrated magnetic entropy (red dots, right y -axis). The solid red line indicates an estimate of the entropy which is missing from the temperature range below 0.35 K. The two dashed gray lines mark the expected entropy values for a $\tilde{S} = 1/2$ and $J = 15/2$ state.

powder average and thus an admixture of the magnetic easy and hard directions. The saturation field of the latter might exceed our experimental accessible range and hence results in the observation of a finite slope for large applied fields. Thus, we refrain from fitting the field-dependent magnetization data.

To further explore the low-temperature magnetism of

the two samples we extracted the magnetic contribution of the specific heat for various applied fields up to 9 T measured down to 0.36 mK. The phononic contribution was subtracted by Lindemann-scaling the specific heat of the non-magnetic analogue TiLuSe₂.

$C_{p,mag}$ of TlErSe₂ (Fig. 5) reveals a sharp peak at 420 mK and zero field. This peak is suppressed by applying an external magnetic field until no sharp specific heat peak is observable down to 0.36 K at 0.5 T. It marks the onset of long-range antiferromagnetic order. Besides the sharp main peak, a faint shoulder is observed, which develops into a broad hump (labeled T^*), shifting toward higher temperatures with increasing fields. This broad feature is typical for quasi 2D systems and indicates the onset of 2D correlations. In addition, a second hump at higher temperatures, i.e., around $T \sim 12$ K (T_{CEF}) is observed. This broad feature originates from the population of higher CEF levels. T_{CEF} remains rather stationary for fields up to 4 T. In this field range both humps merge and become indistinguishable. At an applied field of 9 T the combined maximum is shifted to ~ 17 K.

The corresponding entropy release ΔS_{mag} is presented in Fig. 6 and shows a steep increase corresponding to the sharp specific heat peak of the magnetic phase transition followed by a leveling-off in the low-temperature regime ($T < 6$ K). The plateau-like feature is close to $R \cdot \ln(2)$. This is the expected value for a $\tilde{S} = 1/2$ spin system verifying the ground-state Kramers doublet. With the transition temperature $T_N = 0.420$ K close to the system's limitation it is not possible to capture the full peak. Therefore some of the entropy at low temperatures is not accounted for when integrating over $C_{p,mag}/T$. A rough estimate of this contribution to S_{mag} is given by the red-shaded area above the data points. $C_{p,mag}$ was fitted with $C_{p,mag} \propto T^3$, which expected for an antiferromagnet close to T_N [51]. Above 6 K the released entropy increases steadily approaching $R \cdot \ln(2(15/2) + 1)$ the value of expected for a free Er³⁺ ion.

The magnetic contribution of the specific heat measurement of TiTmSe₂ as a function of temperature is displayed in Fig. 7 for various applied magnetic fields. Throughout the whole temperature range, no sharp anomaly, apart from a small measurement artifact around ~ 0.55 K [52], is observed suggesting the absence of a spontaneous long-range magnetic order phase transition down to ~ 0.5 K. The magnetic contribution of the specific heat exhibits a broad maximum at $T_{max} = 5$ K for magnetic fields below 2 T. With increasing field strength the maximum shifts linearly towards higher temperatures and smears out further. Fig. 8 shows $C_{p,mag}/T$ at zero-field up to ~ 200 K. In the higher temperature regime, another broad feature T_{CEF} is observed at approximately 45 K. The origin of this bump can be related to the higher crystal electric field levels being populated, which is supported by the released entropy in this temperature regime. The obtained magnetic entropy is shown in the same figure. It experiences a plateau-like feature around $R \cdot \ln(2)$ similar to TlErSe₂.

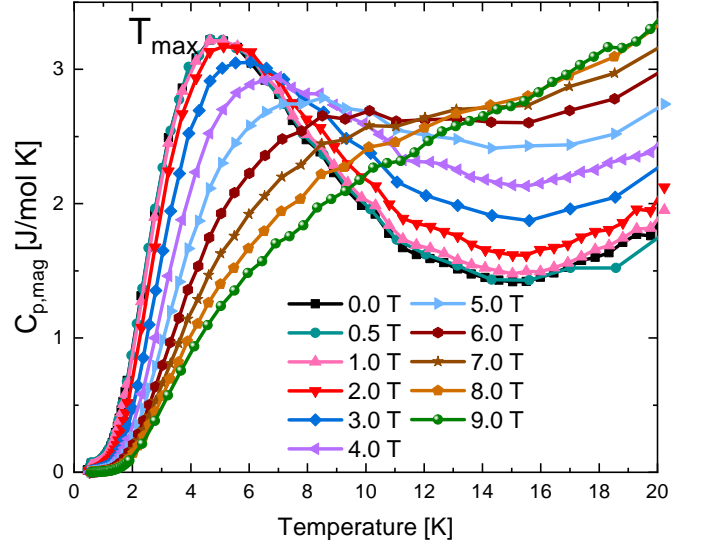


Figure 7. Magnetic contribution of the specific heat $C_{p,mag}$ as a function of temperature of TiTmSe₂ for various applied magnetic fields. T_{max} marks the observed broad maximum which broadens even further for large applied fields.

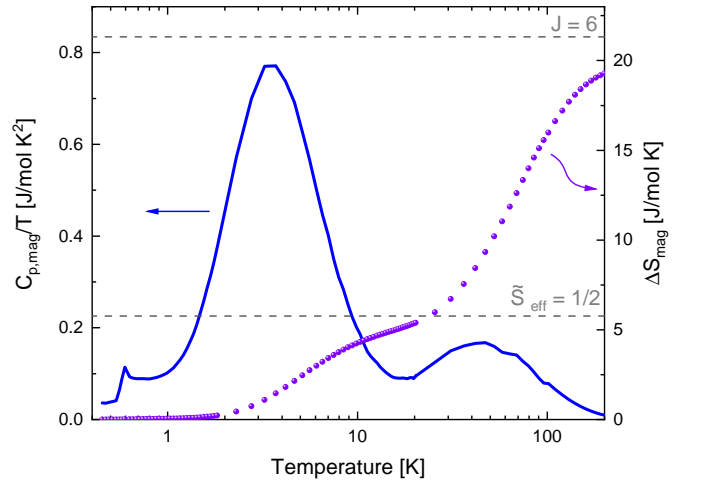


Figure 8. Magnetic contribution of the specific heat divided by temperature $C_{p,mag}/T$ of the zero field measurement (blue solid line, left y -axis) and the corresponding integrated magnetic entropy released (purple dots, right y -axis). The two dashed gray lines mark the expected entropy values for an effective spin $\tilde{S} = 1/2$ and $J = 6$ state.

While this may indicate a $\tilde{S} = 1/2$ regime below ~ 20 K, the entropy released for a Schottky-like anomaly originating from two singlet states is expected to yield the same value, as S depends solely on the ratio of degeneracies g_1/g_0 for a two-level system [51]. Considering the reduction of μ_{eff} for low temperatures as well as the CEF calculations presented below the lowest energy levels are (nonmagnetic) singlet states and thus the second scenario is more plausible for the Tm compound. For elevated temperatures, the entropy approaches the expected

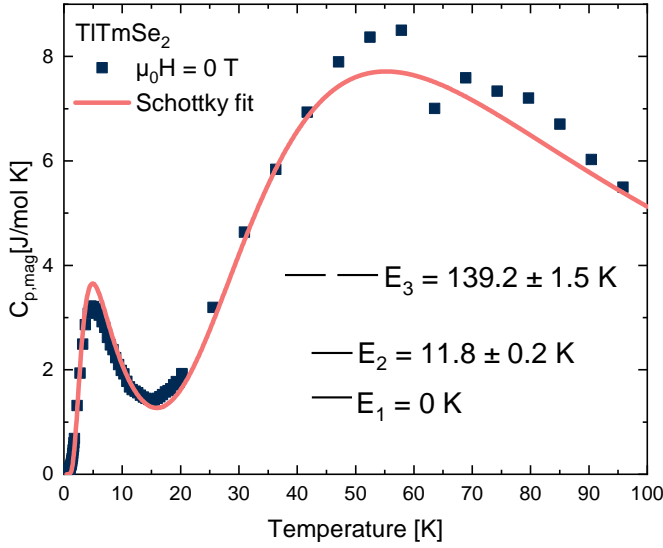


Figure 9. Magnetic contribution of the specific heat of TlTmSe₂ as a function of temperature for zero field. The solid line corresponds to a Schottky fit considering three energy levels [51]. The level scheme is depicted and the data was best described with a degeneracy ratio of 1 : 1 : 2, for the energy levels E_1 , E_2 , and E_3 , respectively.

value for the $J = 6$ $4f$ manifold of a free Tm³⁺.

In Fig. 9 the magnetic contribution of the specific heat was fitted with a Schottky approach using three energy levels E_1 , E_2 , and E_3 , while the first two correspond to the ground and first excited CEF levels the third accounts for higher CEF levels. For the degeneracy g_i of the levels the best fit was obtained with E_1 and E_2 having the same value, and g_3 being twice this value. From this we conclude that the two lowest energy levels are most likely singlet states with an energy gap of 11.8 ± 0.2 K, which is in agreement with the quantum chemical calculations presented below.

In order to understand the different behavior of the two compounds, we performed DFT and quantum chemical calculations. In the DFT calculation both materials are insulators. Fig. 10 a) and b) show the band structures and density of states (DOS) in TlErSe₂ and TlTmSe₂ respectively. The calculated band structures show strong similarities, with almost identical dispersions over the Brillouin zone for both compounds. This is expected as both compounds are isostructural, their crystal structures are similar and their $4f$ electrons can be treated as core electrons.

The top of the valence bands in both materials consists predominantly of p -states of Se. The conduction band electrons originate from both the d -electron orbitals of Er(Tm) and the p -electrons of Tl. The resulting indirect gap is about 0.74 eV (TlErSe₂) and 0.69 eV (TlTmSe₂). This structure ensures that the magnetic response comes entirely from localised $4f$ electrons.

For insights into the $4f$ electronic structures we carried out quantum chemical calculations. The low-energy

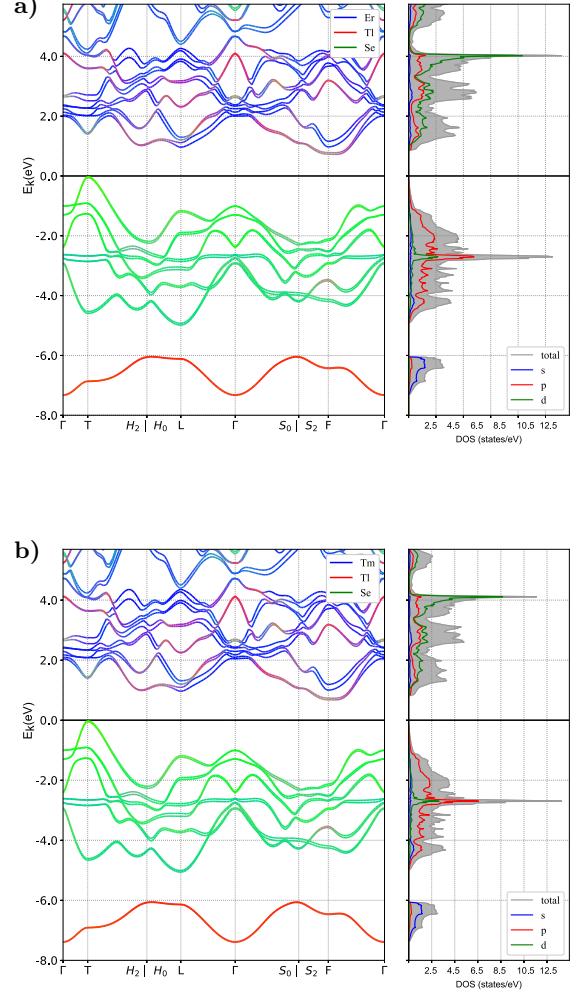


Figure 10. Band structure and density of states of TlErSe₂ a) and TlTmSe₂ b).

NEVPT2 spectrum of TlErSe₂ is defined by a group of eight SO doublets with relative energies of 0, 6.5, 7.4, 8.7, 11.3, 30.4, 32.4, and 33.4 meV, related to the $J = 15/2$ free-ion ground-state term. Other excited SO states require excitation energies of at least 0.75 eV. Notably, the NEVPT2 treatment brings significant corrections to the CASSCF relative energies, an aspect that is detailed in the Appendix (Tab. II). The lowest excited state lies somewhat lower compared to the case of $4f^{13}$ ions in similar crystalline environment [18, 39].

The low-energy MRCI spectrum for the TlTmSe₂ compound is defined by a group of five SO singlets and four SO doublets with relative energies of 0, 0.8, 3.5, 5.1, 9.0, 12.9, 18.7, 19.1, and 21.7 meV, related to the $J = 6$ free-ion ground-state term. Other excited SO states are located above 0.95 eV. The MRCI treatment brings significant corrections to the CASSCF excitation energies, as presented in Table III. In other $4f^{12}$ triangular-lattice

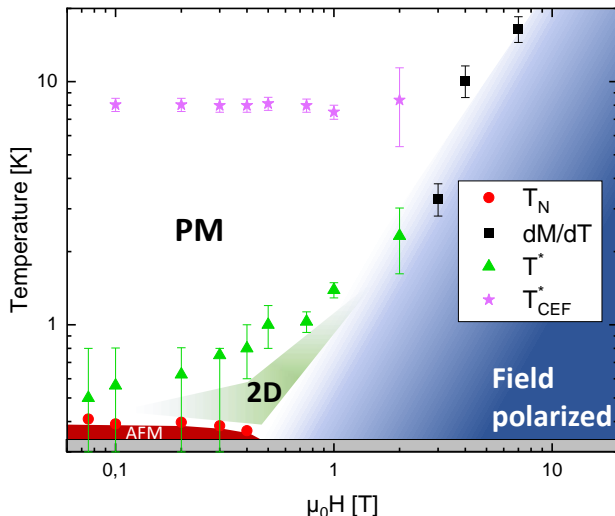


Figure 11. Field-temperature phase diagram of TlErSe₂ on a Log-Log scale. Marked are T_N (red circles) corresponding to the sharp peak and the shoulder (light green triangles) which develops into a broad bump (pink stars) observed in $C_{p,mag}$ as well as the onset of saturation as measured by high field susceptibility (black squares); for more information see text. The colored areas are meant as guides-to-the-eye. The grey shaded area below marks the temperature limit of the device.

compounds, e.g., KTmSe₂ [8] and NaTmTe₂ [53], the experimentally determined first excited state is at 1.2 and 2.9 meV, respectively.

IV. DISCUSSION AND SUMMARY

Our results show that TlErSe₂ is an example of a magnetically long-range ordered triangular lattice antiferromagnet governed by its spin $\tilde{S} = 1/2$ Kramers doublet ground-state, similar to NaErSe₂ [46], NaErS₂ [54], KCeSe₂ [49, 55], KErSe₂ [46, 56] or KYbSe₂ [57], contrasting putative quantum spin liquid candidates like NaYbSe₂ [14, 20], NaYbO₂ [58], KYbS₂ [59] or CsYbSe₂ [60]. While both kinds of behavior are observed within the delafossite family a clear tuning parameter remains unclear and under debate. However, it is evident that anisotropic exchange plays a significant role. For similar Er³⁺ based compounds both easy plane (XY) anisotropy (ErMgGaO₄ [61], K₃Er(VO₄)₂ [62], Er₂Ti₂O₇, NaErSe₂ [46], CsErSe₂ [50]) and Ising anisotropy (Ba₃ErB₉O₁₈ [63]) were reported, motivating follow-up studies of single crystalline samples.

Nonetheless, given the temperature range and the large total angular momentum of $J = \pm 15/2$ associated with the Er³⁺ ground state doublet, here, dipolar interactions can be a driving factor for the onset of long-range magnetic order. Following this the most likely ordering type would be a stripe order with the moments pointing along the Er – Er bond axis.

In addition to the pronounced peak at T_N , a shoulder-

like feature was observed evolving into a broad hump at larger fields (see Fig. 11). Due to the delafossites crystal structure, i.e., stacked rare-earth ion triangular layers well separated by A^+ spacer layers, the hierarchy of the magnetic couplings (\mathcal{J}) closely resembles quasi-2D systems with $\mathcal{J}_{intra\text{layer}} \gg \mathcal{J}_{inter\text{layer}}$. Here, these broad features appearing just before a magnetically ordered state forms correspond to 2D correlations [64].

While the work by Liu et al. [65] proposed numerous ordered states for non-Kramers doublets on a triangular lattice, no sign indicating long-range magnetic order was found in TlTmSe₂ down to 360 mK. These findings are in line with reports on related compounds such as KTmSe₂ [8], NaTmSe₂ [66] or LiTmSe₂ [66]. Our quantum chemical calculations suggest a sizable energy gap of 0.8 or 1.2 meV between the two lowest singlet states, CASSCF or MRCI respectively. In agreement with this, fitting the low temperature specific heat with a two level Schottky system yields an energy gap and degeneracy ratio of the two lowest level of 11.8 K and 1 : 1, respectively. Following, it is likely, that the absence of a sharp ordering transition in TlTmSe₂ can be attributed to the non-magnetic nature of its ground state singlet and the comparably large energy gap to the next higher CEF level.

In summary, we report the synthesis of high quality polycrystalline TlMSe₂ (M : Er and Tm) samples. While the erbium compound shows clear signs of the presence of a long-range antiferromagnetic ordered phase below 420 mK, no such signs were found for TlTmSe₂. This profound difference in magnetic properties is attributed to the distinct difference in the CEF-level structure. For TlErSe₂ the $\tilde{S} = 1/2$ kramers doublet ground state of the Er³⁺ ions most likely is dominated by contributions of large $|m_J\rangle$ which results in a sizable dipolar coupling, strong enough to stabilize long-range order in the ³He temperature range. With this coupling mechanism not present in the well separated non-magnetic singlet ground state of the Tm³⁺ ions, here, no long-range order phase can form.

V. ACKNOWLEDGEMENTS

We acknowledge financial support from the German Research Foundation (DFG) within the SFB 1143 Correlated Magnetism From Frustration to Topology, project-id 247310070 (Projects B01, B03 and A05) and project No.390858490 (Würzburg-Dresden Cluster of Excellence on Complexity and Topology in Quantum Matter – ct.qmat, EXC 2147) We appreciate the ICP-OES measurements by Dr. Gudrun Auffermann (MPI-CPFS Dresden). D.V.E. and A.N. thank M. Richter for discussions and U. Nitzsche for technical support and acknowledge financial support from the DFG, projects 529677299, 455319354. P.B. and L.H. thank T. Petersen for discussions, U. Nitzsche for technical support, and the DFG (Project No. 441216021) for financial support.

- [1] C. Kim, S. Kim, P. Park, T. Kim, J. Jeong, S. Ohira-Kawamura, N. Murai, K. Nakajima, A. L. Chernyshev, M. Mourigal, S.-J. Kim, and J.-G. Park, *Nature Physics* **19**, 1624–1629 (2022).
- [2] P. Bhattacharyya, N. A. Bogdanov, S. Nishimoto, S. D. Wilson, and L. Hozoi, *npj Quantum Materials* **8**, 10.1038/s41535-023-00582-7 (2023).
- [3] T. Xie, S. Gozel, J. Xing, N. Zhao, S. M. Avdoshenko, L. Wu, A. S. Sefat, A. L. Chernyshev, A. M. Läuchli, A. Podlesnyak, and S. E. Nikitin, *Phys. Rev. Lett.* **133**, 096703 (2024).
- [4] Y. Shen, C. Liu, Y. Qin, S. Shen, Y.-D. Li, R. Bewley, A. Schneidewind, G. Chen, and J. Zhao, *Nat. Commun.* **10**, 4530 (2019).
- [5] Z. Dun, M. Daum, R. Baral, H. E. Fischer, H. Cao, Y. Liu, M. B. Stone, J. A. Rodriguez-Rivera, E. S. Choi, Q. Huang, H. Zhou, M. Mourigal, and B. A. Frandsen, *Phys. Rev. B* **103**, 064424 (2021).
- [6] Z. Hu, Z. Ma, Y.-D. Liao, H. Li, C. Ma, Y. Cui, Y. Shang-guan, Z. Huang, Y. Qi, W. Li, Z. Y. Meng, J. Wen, and W. Yu, *Nat. Commun.* **11**, 5631 (2020).
- [7] C. Liu, C.-J. Huang, and G. Chen, *Physical Review Research* **2**, 043013 (2020).
- [8] S. Zheng, H. Wo, Y. Gu, R. L. Luo, Y. Gu, Y. Zhu, P. Steffens, M. Boehm, Q. Wang, G. Chen, and J. Zhao, *Phys. Rev. B* **108**, 054435 (2023).
- [9] Y. Da Liao, H. Li, Z. Yan, H.-T. Wei, W. Li, Y. Qi, and Z. Y. Meng, *Phys. Rev. B* **103**, 104416 (2021).
- [10] S. V. Isakov and R. Moessner, *Phys. Rev. B* **68**, 104409 (2003).
- [11] M. Baenitz, P. Schlender, J. Sichelschmidt, Y. A. Onyukienko, Z. Zangeneh, K. M. Ranjith, R. Sarkar, L. Hozoi, H. C. Walker, J.-C. Orain, H. Yasuoka, J. van den Brink, H. H. Klauss, D. S. Inosov, and T. Doert, *Phys. Rev. B* **98**, 220409 (2018).
- [12] K. M. Ranjith, D. Dmytriieva, S. Khim, J. Sichelschmidt, S. Luther, D. Ehlers, H. Yasuoka, J. Wosnitza, A. A. Tsirlin, H. Kühne, and M. Baenitz, *Phys. Rev. B* **99**, 180401 (2019).
- [13] J. Sichelschmidt, P. Schlender, B. Schmidt, M. Baenitz, and T. Doert, *J. Condens. Matter Phys.* **31**, 205601 (2019).
- [14] K. M. Ranjith, S. Luther, T. Reimann, B. Schmidt, P. Schlender, J. Sichelschmidt, H. Yasuoka, A. M. Strydom, Y. Skourski, J. Wosnitza, H. Kühne, T. Doert, and M. Baenitz, *Phys. Rev. B* **100**, 224417 (2019).
- [15] L. Ding, P. Manuel, S. Bachus, F. Grubler, P. Gegenwart, J. Singleton, R. D. Johnson, H. C. Walker, D. T. Adroja, A. D. Hillier, and A. A. Tsirlin, *Phys. Rev. B* **100**, 144432 (2019).
- [16] M. M. Bordelon, E. Kenney, C. Liu, T. Hogan, L. Posthuma, M. Kavand, Y. Lyu, M. Sherwin, N. P. Butch, C. Brown, *et al.*, *Nat. Phys.* **15**, 1058 (2019).
- [17] M. M. Bordelon, C. Liu, L. Posthuma, P. M. Sarte, N. P. Butch, D. M. Pajerowski, A. Banerjee, L. Balents, and S. D. Wilson, *Phys. Rev. B* **101**, 224427 (2020).
- [18] Z. Zhang, X. Ma, J. Li, G. Wang, D. T. Adroja, T. P. Perring, W. Liu, F. Jin, J. Ji, Y. Wang, Y. Kamiya, X. Wang, J. Ma, and Q. Zhang, *Phys. Rev. B* **103**, 035144 (2021).
- [19] P.-L. Dai, G. Zhang, Y. Xie, C. Duan, Y. Gao, Z. Zhu, E. Feng, Z. Tao, C.-L. Huang, H. Cao, A. Podlesnyak, G. E. Granroth, M. S. Everett, J. C. Neufeind, D. Voneshen, S. Wang, G. Tan, E. Morosan, X. Wang, H.-Q. Lin, L. Shu, G. Chen, Y. Guo, X. Lu, and P. Dai, *Phys. Rev. X* **11**, 021044 (2021).
- [20] W. Liu, Z. Zhang, J. Ji, Y. Liu, J. Li, X. Wang, H. Lei, G. Chen, and Q. Zhang, *Chin. Phys. Lett.* **35**, 117501 (2018).
- [21] T. Fujii, M. Pillaca, F. Bärthel, J. Sichelschmidt, S. Luther, H. Rosner, A. M. Strydom, J. Wosnitza, H. Kühne, T. Doert, and M. Baenitz, *Phys. Rev. B* **112**, 024426 (2025).
- [22] B. R. Ortiz, M. M. Bordelon, P. Bhattacharyya, G. Pokharel, P. M. Sarte, L. Posthuma, T. Petersen, M. S. Eldeeb, G. E. Granroth, C. R. Dela Cruz, S. Calder, D. L. Abernathy, L. Hozoi, and S. D. Wilson, *Phys. Rev. Mater.* **6**, 084402 (2022).
- [23] S. Kabré, M. Julien-Pouzol, and M. Guittard, *Bulletin de la société chimique de France, Partie I*, 1881 (1974).
- [24] M. Duczmal and L. Pawlak, *J. Alloys Compd.* **209**, 271 (1994).
- [25] M. Duczmal and L. Pawlak, *J. Alloys Compd.* **225**, 181 (1995).
- [26] T. Ferreira, J. Xing, L. D. Sanjeewa, and A. S. Sefat, *Front. Chem.* **8**, 127 (2020).
- [27] A. A. Coelho, *J. Appl. Crystallogr.* **51**, 210 (2018).
- [28] A. A. Coelho, *Topas academic v4.1 technical reference* (2020).
- [29] G. Kresse and D. Joubert, *Phys. Rev. B* **59**, 1758 (1999).
- [30] G. Kresse and J. Furthmüller, *Phys. Rev. B* **54**, 11169 (1996).
- [31] G. Kresse and J. Hafner, *Phys. Rev. B* **48**, 13115 (1993).
- [32] S. P. Ong, W. D. Richards, A. Jain, G. Hautier, M. Kocher, S. Cholia, D. Gunter, V. L. Chevrier, K. A. Persson, and G. Ceder, *Computational Materials Science* **68**, 314 (2013).
- [33] F. Neese, *WIREs Comput. Mol. Sci.* **12**, e1606 (2022).
- [34] F. Neese, F. Wennmohs, U. Becker, and C. Riplinger, *J. Chem. Phys.* **152**, 224108 (2020).
- [35] H.-J. Werner, P. J. Knowles, G. Knizia, F. R. Manby, and M. Schütz, *WIREs Comput. Mol. Sci.* **2**, 242 (2012).
- [36] M. Klintonberg, S. Derenzo, and M. Weber, *Comp. Phys. Commun.* **131**, 120 (2000).
- [37] S. E. Derenzo, M. K. Klintonberg, and M. J. Weber, *J. Chem. Phys.* **112**, 2074 (2000).
- [38] P. Bhattacharyya, U. K. Rößler, and L. Hozoi, *Phys. Rev. B* **105**, 115136 (2022).
- [39] P. Bhattacharyya and L. Hozoi, *Phys. Rev. B* **105**, 235117 (2022).
- [40] T. Helgaker, P. Jørgensen, and J. Olsen, *Molecular Electronic Structure Theory* (John Wiley & Sons, Chichester, 2000).
- [41] P. J. Knowles and H.-J. Werner, *Theor. Chim. Acta* **84**, 95 (1992).
- [42] C. Angeli, R. Cimraglia, S. Evangelisti, T. Leininger, and J.-P. Malrieu, *J. Chem. Phys.* **114**, 10252 (2001).
- [43] M. Duczmal, *Struktura, właściwości magnetyczne i pole krystaliczne w potrójnych chalcogenkach lantanowców i talu TlLnX₂ (X (Oficyna Wydawnicza Politechniki Wrocławskiej, 2003).*

- [44] K. Momma and F. Izumi, *J. Appl. Crystallogr.* **44**, 1272 (2011).
- [45] N. W. Ashcroft and N. D. Mermin, *Solid State Physics* (Holt-Saunders, 1976).
- [46] J. Xing, L. D. Sanjeewa, J. Kim, W. R. Meier, A. F. May, Q. Zheng, R. Custelcean, G. Stewart, and A. S. Sefat, *Physical Review Materials* **3**, 114413 (2019).
- [47] A. P. Ramirez, G. P. Espinosa, and A. S. Cooper, *Phys. Rev. Lett.* **64**, 2070 (1990).
- [48] B. Schmidt, J. Sichelschmidt, K. M. Ranjith, T. Doert, and M. Baenitz, *Phys. Rev. B* **103**, 214445 (2021).
- [49] G. Bastien, B. Rubrecht, E. Haeussler, P. Schlender, Z. Zangeneh, S. Avdoshenko, R. Sarkar, A. Alfonso, S. Luther, Y. A. Onykiienko, H. C. Walker, H. Kühne, V. Grinenko, Z. Guguchia, V. Kataev, H. H. Klauss, L. Hozoi, J. van den Brink, D. S. Inosov, B. Büchner, A. U. B. Wolter, and T. Doert, *SciPost Phys.* **9**, 041 (2020).
- [50] A. Scheie, V. O. Garlea, L. D. Sanjeewa, J. Xing, and A. S. Sefat, *Phys. Rev. B* **101**, 144432 (2020).
- [51] E. S. R. Gopal, *Specific heats at low temperatures* (1966).
- [52] The artifact originates from a faulty calibration file of the platform thermometer resistance provided by the manufacturer. The problem was fixed before proceeding with the erbium and lutetium based compounds.
- [53] S. Zheng, Y. Gu, Y. Gu, Z. Kao, Q. Wang, H. Wo, Y. Zhu, F. Liu, L. Wu, J. Sheng, J. Chang, S. Ohira-Kawamura, N. Murai, C. Niedermayer, D. G. Mazzone, G. Chen, and J. Zhao, *Phys. Rev. B* **109**, 075159 (2024).
- [54] S. Gao, F. Xiao, K. Kamazawa, K. Ikeuchi, D. Biner, K. W. Krämer, C. Rüegg, and T. hisa Arima, *Phys. Rev. B* **102**, 024424 (2020).
- [55] A. A. Kulbakov, S. M. Avdoshenko, I. Puente-Orench, M. Deeb, M. Doerr, P. Schlender, T. Doert, and D. S. Inosov, *J. Condens. Matter Phys.* **33**, 425802 (2021).
- [56] J. Xing, K. M. Taddei, L. D. Sanjeewa, R. S. Fishman, M. Daum, M. Mourigal, C. dela Cruz, and A. S. Sefat, *Phys. Rev. B* **103**, 144413 (2021).
- [57] A. O. Scheie, E. A. Ghioldi, J. Xing, J. A. M. Paddison, N. E. Sherman, M. Dupont, L. D. Sanjeewa, S. Lee, A. J. Woods, D. Abernathy, D. M. Pajerowski, T. J. Williams, S.-S. Zhang, L. O. Manuel, A. E. Trumper, C. D. Pemmaraju, A. S. Sefat, D. S. Parker, T. P. Devereaux, R. Movshovich, J. E. Moore, C. D. Batista, and D. A. Tennant, Witnessing quantum criticality and entanglement in the triangular antiferromagnet KYbSe₂ (2023), [arXiv:2109.11527 \[cond-mat.str-el\]](https://arxiv.org/abs/2109.11527).
- [58] J. Wu, J. Li, Z. Zhang, C. Liu, Y. H. Gao, E. Feng, G. Deng, Q. Ren, Z. Wang, R. Chen, J. Embs, F. Zhu, Q. Huang, Z. Xiang, L. Chen, Y. Wu, E. S. Choi, Z. Qu, L. Li, J. Wang, H. Zhou, Y. Su, X. Wang, G. Chen, Q. Zhang, and J. Ma, *Quantum Frontiers* **1**, 13 (2022).
- [59] R. Iizuka, S. Michimura, R. Numakura, Y. Uwatoko, and M. Kosaka, in *JPS Conf. Proc.* (2020) p. 011097.
- [60] J. Xing, L. D. Sanjeewa, J. Kim, G. R. Stewart, M.-H. Du, F. A. Reboredo, R. Custelcean, and A. S. Sefat, *ACS Mater. Lett.* **2**, 71 (2019).
- [61] Y. Cai, C. Lygouras, G. Thomas, M. N. Wilson, J. Beare, S. Sharma, C. A. Marjerrison, D. R. Yahne, K. A. Ross, Z. Gong, Y. J. Uemura, H. A. Dabkowska, and G. M. Luke, *Phys. Rev. B* **101**, 094432 (2020).
- [62] D. R. Yahne, L. D. Sanjeewa, A. S. Sefat, B. S. Stadelman, J. W. Kolis, S. Calder, and K. A. Ross, *Phys. Rev. B* **102**, 104423 (2020).
- [63] J. Khatua, M. Pregelj, A. Elghandour, Z. Jagličić, R. Klingeler, A. Zorko, and P. Khuntia, *Phys. Rev. B* **106**, 104408 (2022).
- [64] P. Sengupta, A. W. Sandvik, and R. R. Singh, *Physical Review B* **68**.
- [65] C. Liu, Y.-D. Li, and G. Chen, *Physical Review B* **98**, 045119 (2018).
- [66] M. Boswell, C. Peng, and W. Xie, *Journal of Applied Physics* **137**, 183901 (2025).
- [67] D. Aravena, F. Neese, and D. A. Pantazis, *J. Chem. Theory Comput.* **12**, 1148 (2016).
- [68] W. A. de Jong, R. J. Harrison, and D. A. Dixon, *J. Chem. Phys.* **114**, 48 (2001).
- [69] M. Dolg, H. Stoll, and H. Preuss, *J. Chem. Phys.* **90**, 1730 (1989).
- [70] W. Küchle, M. Dolg, H. Stoll, and H. Preuss, *Mol. Phys.* **74**, 1245 (1991).
- [71] X. Cao and M. Dolg, *J. Chem. Phys.* **115**, 7348 (2001).
- [72] X. Cao and M. Dolg, *J. Mol. Struct.: THEOCHEM* **581**, 139 (2002).
- [73] H. Stoll, B. Metz, and M. Dolg, *J. Comput. Chem.* **23**, 767 (2002).
- [74] M. Dolg, H. Stoll, A. Savin, and H. Preuss, *Theor. Chim. Acta* **75**, 173 (1989).
- [75] M. Dolg, H. Stoll, and H. Preuss, *Theor. Chim. Acta* **85**, 441 (1993).

APPENDIX

We employed the SARC2-DKH-QZVP basis set (BS) for the central $\text{Er}^{3+} 4f^{11}$ ion [67] and all-electron relativistic BSs of triple- ζ quality for the Se ligands [68] of the ErSe_6 octahedron; within the buffer cationic region between the reference ErSe_6 octahedron and the point-charge matrix, large-core pseudopotentials were utilized for the six Er^{3+} [69] and 12 Tl^+ [70] species.

Negligible changes in the relative energies were observed if only 30 spin quartets and 43 spin doublets instead of all possible states associated with the $\text{Er}^{3+} 4f^{11}$ configuration were considered in the quantum chemical calculations (see Table IV).

For the central $\text{Tm}^{3+} 4f^{12}$ ion energy-consistent quasirelativistic pseudopotentials (ECP28MWB) [69] and Gaussian-type valence BSs of effective quadruple- ζ quality [71, 72] were employed, whereas we used relativistic pseudopotentials (ECP46MDF) [73] along with (6s6p)/[4s4p] valence BSs for the six Se ligands of the central TmSe_6 octahedron.

Large-core pseudopotentials including the $4f$ subshell in the core (ECP58MWB) [74, 75] were adopted for the six adjacent Tm sites, along with (4s3p)/[2s1p] valence BSs. We considered large-core pseudopotentials for the 12 Tl nearest neighbors (ECP78MWB) [70] with (4s3p)/[2s1p] valence BSs.

Table II. Low-energy $4f$ -site multiplet structure in TlErSe_2 ($J = 15/2$ -like levels); relative energies of the lowest eight SO doublets (meV). All possible states derived from the $4f^{11}$ configuration entered the SO treatment.

Levels	CASSCF+SOC	NEVPT2+SOC
1	0.0	0.0
2	0.9	6.5
3	5.0	7.4
4	6.0	8.7
5	7.0	11.3
6	18.3	30.4
7	20.8	32.4
8	22.3	33.4

Table III. Low-energy $4f$ -site multiplet structure in TlTmSe_2 ($J = 6$ -like levels); relative energies in meV. The lowest 11 spin triplets and nine spin singlets derived from the $4f^{12}$ configuration entered the SO treatment. The levels joined by brackets are doublets not split by the crystal field.

Levels	CASSCF+SOC	MRCI+SOC
1	0.0	0.0
2	1.2	0.8
3] 4]	1.9	3.5
5] 6]	3.3	5.1
7	6.8	9.0
8	10.2	12.9
9	14.0	18.7
10] 11]	14.7	19.1
12] 13]	17.2	21.7

Table IV. Low-energy $4f$ -site multiplet structure (meV) in TiErSe_2 at NEVPT2+SOC level, dependence on the number of states considered in the SO computations. Q and D stand for quartet and doublet spin multiplicities, respectively.

Levels	(30 Q + 43 D) ^a	(35 Q + 112 D)
1	0.0	0.0
2	6.5	6.5
3	7.4	7.4
4	8.6	8.7
5	11.2	11.3
6	30.4	30.4
7	32.4	32.4
8	33.4	33.4

^a Orbitals as employed in the adjacent column were used.

Table V. Low-energy $4f$ -site multiplet structure (meV) in TiTmSe_2 at CASSCF+SOC level, dependence on the number of states considered in the SO computations (relative energies in meV). T and S stand for triplet and singlet spin multiplicities, respectively.

Levels	(11 T + 9 S) ^a	(21 T + 28 S)
1	0.0	0.0
2	1.2	1.2
3]	1.9	1.9
4]		
5]	3.3	3.2
6]		
7	6.8	6.6
8	10.2	10.0
9	14.0	13.8
10]	14.7	14.4
11]		
12]	17.2	16.9
13]		

^a Orbitals as employed in the adjacent column were used.